International Journal of Engineering and Technology Innovation, vol. 12, no. 4, 2022, pp. 275-287

Prediction of Wind Turbine Airfoil Performance Using Artificial Neural Network and CFD Approaches

Mojtaba Moshtaghzadeh[1,*], Mohammad Reza Aligoodarz[2]

[1]Department of Mechanical and Materials Engineering, Florida International University, Miami, Florida, USA

[2]Department of Mechanical and Materials Engineering, Shahid Rajaee Teacher Training University, Tehran, Iran

Received 21 March 2022; received in revised form 13 May 2022; accepted 14 May 2022

DOI: https://doi.org/10.46604/ijeti.2022.9735

Abstract

To achieve the highest energy level from a wind turbine, the prediction of its performance is essential. This study investigates the aerodynamic performance of different airfoils, which are frequently used in wind farms. The computational fluid dynamics method based on the finite-volume approach is utilized, and a steady-state flow with the transition regime is considered in this study. A developed artificial neural network is used to reduce the computational time. The results indicates that the trained algorithm could accurately predict the airfoil efficiency with less than 2% error on the training set and fewer than 3% error on the test set. The results agree with the experimental results; this analysis accurately predicts wind turbine performance by selecting the blade's airfoil. This study provides a reference for a broader range of using these airfoils in wind farms.

Keywords: wind turbine, ANN, CFD, wind speed, airfoil

1. Introduction

The wind is clean energy that most developed countries have been using in recent decades. Using this energy has been getting more common worldwide since it can be discovered anywhere. Moreover, it is a valuable renewable energy source that does not contribute to global warming. It explains why this energy has a priority among renewable energies in academic and industrial studies. While researchers study utilizing much more renewable energies, they should consider needed technologies, costs, and challenges.

Due to the fast growth of wind energy implementations and the lack of wind sources worldwide, their efficiency has attracted more attention. Hence, it is critical to optimize the efficiency of turning wind energy into mechanical energy to make these applications cost-effective. Computational fluid dynamics (CFD) is one of the most efficient approaches for developing and improving the next generation of wind turbines. In order to predict the performance of rotary machines, numerical approaches solve the two- or three-dimensional governing equations to obtain the applied or generated forces in the system [1-2]. The aerodynamic efficiency (L/D) should be calculated to find the performance of a used airfoil in a wind turbine. The highest efficiency of a wind turbine can be achieved by increasing the sliding ratio (lift to drag coefficient) and finding the optimum aerodynamic design parameter [3].

Manwell et al. [4] presented the maximum power coefficient, C_p, for an optimum airfoil. They showed that the wind turbine power decreases significantly by increasing the drag force. In another study, Sayed et al. [5] studied the NREL airfoil family performance based on wind conditions in Egypt. They found the airfoils S825, S826, S830, and S831 are suitable for that condition. Flexible cambered airfoils can enhance the turbine performance by changing the sliding ratio. Although a thicker airfoil needs an enormous load to increase the lift coefficient, it has significant resistance to deformation. On the other

* Corresponding author. E-mail address: mmosh009@fiu.edu

hand, the composite material of blades has a substantial effect on the performance of a wind turbine. Hua et al. [6] designed an inspired-bird wing airfoil and used a numerical method to evaluate and compare the performance. It is shown that changing airfoil configuration can improve performance significantly.

In order to improve the aerodynamic modeling of a wind turbine, the nature and physics of the flow should be considered around the blades [7]. A comprehensive numerical simulation has been done to study wind turbine performance using the CFD method in the work of Dai et al. [8]. Clainche et al. [9] proposed a reduced-order model to find the flow behavior around wind turbines in a turbulent regime. Pesmajoglou and Graham [10] predicted aerodynamic forces for different yaw angles. They used the free vortex lattice model to simulate the flow. Churchfield et al. [11] performed a numerical analysis to find the effects of atmospheric stability and surface roughness on wind turbine dynamics. They presented a methodology to study multiple turbines in the atmospheric and wake conditions.

Over the past decades, there has been a sustained research activity in wind turbine performance. According to the literature, most studies have been focused on turbulence flows and the high wind speed range. Ahmadi-Baloutaki et al. [12] investigated the effect of free-stream turbulence on a NACA0015 airfoil. They presented that the free-stream turbulence in the stall region can improve the aerodynamic performance. In addition, Wang et al. [13] studied the effect of the unsteady separation of a turbulence transition flow on the NACA0012 airfoil performance. They compared the SST and K-ω models results with experimental data and discussed the development of the dynamic stall. In addition, different turbulence models were examined by Yao and Yuan [14] on the NACA0018 airfoil. Therefore, more research needs to be performed to show how the laminar and transition regimes can affect the wind turbine performance at the lower wind speed range.

Studying the effect of geometric parameters on the aerodynamic performance of wind turbines over a vast and continuous range is difficult to perform. Not only do complex models demand increasing computational time and more powerful computing resources, but also producing the models is burdensome. Therefore, artificial neural network (ANN) is one feasible technique for reducing the computational time of numerical studies. Recent breakthroughs in artificial intelligence have improved the neural network method's capabilities in various disciplines, including electromagnetics [15], multi-phase flow [16], etc. Nielson et al. [17] used the ANN approach to predict the wind turbine power by generating multi-parameters. Luna et al. [18] trained different ANN architectures to predict the fatigue failure of a wind turbine. Saenz-Aguirre et al. [19] employed ANN and CFD approaches to improve the achievable aerodynamic energy of a wind turbine using Gurney flap flow control. Salem et al. [20] showed how the neural network fitting function in the pitch angle control system could provide a viable and appropriate controlling action and enable the wind turbine to obtain the required power curve. Cappugi et al. [21] used ANN to predict the loss of harvested energy from wind turbines because of erosion in the leading edge of blades. In conclusion, the ANN approach can be used for a wide range of parameters and keeps the computational time efficient.

This study explores the effect of airfoil geometry and aerodynamic parameters on the efficiency of a wind turbine. The ANN and CFD approaches are employed for this investigation. Five different airfoils are selected, which are frequently used in wind farms. It is sought the airfoil with the highest efficiency at different angles of attack (AOA). In addition, this study has been performed at a wide range of wind speeds. The literature focuses on the fully developed turbulent flow, but the laminar, transition, and turbulence flows are considered in this study. This numerical study is performed using ANSYS and is verified by comparing the experimental results.

2. Methodology

2.1. Theory

The dimensionless lift and drag coefficients should be used to find the aerodynamics loads on airfoils. These forces are dependent on the airfoil profile and AOA, and their coefficients are as follows [5]:

$$C_L = \frac{L}{0.5\rho V^2 A} \tag{1}$$

$$C_D = \frac{D}{0.5\rho V^2 A} \tag{2}$$

where L and D are the lift and drag forces, respectively. ρ, V, and A are the air density, wind speed, and cross-sectional area of the airfoil, respectively. The sliding ratio is defined as [5]:

$$\varepsilon = \frac{C_L}{C_D} = \frac{L}{D} \tag{3}$$

To study a flow using the finite volume method, mass and momentum conservation equations must be considered in a discretized flow domain [22].

$$\frac{\partial}{\partial x}(\rho uu) + \frac{\partial}{\partial y}(\rho vu) = \frac{\partial}{\partial x}(\mu \frac{\partial u}{\partial x}) + \frac{\partial}{\partial y}(\mu \frac{\partial u}{\partial y}) - \frac{\partial p}{\partial x} + S_u \tag{4}$$

$$\frac{\partial}{\partial x}(\rho uv) + \frac{\partial}{\partial y}(\rho vv) = \frac{\partial}{\partial x}(\mu \frac{\partial v}{\partial x}) + \frac{\partial}{\partial y}(\mu \frac{\partial v}{\partial y}) - \frac{\partial p}{\partial y} + S_v \tag{5}$$

$$\frac{\partial}{\partial x}(\rho u) + \frac{\partial}{\partial y}(\rho v) = 0 \tag{6}$$

where u and v are the velocity components, p is the pressure field, and μ is the dynamic fluid viscosity coefficient on the domain. The effects of surface stresses due to internal sources (associated with the destruction and creation) are denoted with S_u and S_v in each direction. The Michel method [23] is a verified model based on the experimental results that present the local transition point with modified momentum thickness values. The following statement represents the transition from a laminar flow to a turbulent flow [24-25]:

$$Re_{trans} = 1.174\left(1 + \frac{22400}{Re_x}\right) Re_x^{0.46} \tag{7}$$

Re_x is the Reynolds number calculated from the stagnation point, and Re_{trans} is introduced as the momentum thickness Reynolds number.

2.2. Artificial neural network

The developed ANN includes one input layer, two hidden layers, and one output layer in this study. The input layer consists of a 525 × 3 matrix, representing 525 samples of the obtained CFD results with three input parameters, including selected airfoil, wind speed, and AOA. The input variables are normalized to the range [0,1] to offer the ANN additional robustness. The first and subsequent neuron layers process the collected input data to form the desired output. The output layer is presented as a 525 × 1 vector, which estimates the efficiency of used airfoils in the wind turbine (sliding ratio) [15].

In the feedforward technique, the input layer sends input with associated weights to the hidden layer. Each neuron in a hidden layer produces and delivers output to the next layer as the weighted sum of the inputs. The hyperbolic tangent sigmoid function is defined as follows [15, 26]:

$$\sigma_{tansig}(u) = \frac{2}{1+e^{-2u}} - 1 \tag{8}$$

It serves as an activating function within the neurons of the hidden layers. As a result, the following is the output created and passed by each neuron in the network [15, 26]:

$$y_j = \sigma(u_j) = \sigma\left(\sum_i w_{ij} x_i + b_j\right) \tag{9}$$

where y_j is the output generated and passed by a neuron in the jth layer, x_i is the input the neuron gets from its previous layer, the ith layer, and σ is the activation function acting on the output. w_{ij} is the corresponding interconnected weight between the node in the jth layer and its previous node in the ith layer, and b_j is the bias. The backpropagation algorithm, also known as BP, determines the optimum values of w_{ij} and b_j within the network, wherein the ultimate calculated error in the output layer after each iteration on the training dataset is propagated backward from the output layer to the hidden layers, and eventually to the input layer [26]. In each iteration, the root mean square (RMS) of the error determined at the output layer is simply defined as [15, 26]:

$$RMS_{error} = \sqrt{\frac{1}{n}\sum_{k=1}^{n}(e_k)^2} \tag{10}$$

where n is the number of samples in the training dataset, and e_k is the output layer's error:

$$e_k = | Estimated(\varepsilon_k) - Actual(\varepsilon_k) | \tag{11}$$

The BP algorithm employs the gradient descent concept to minimize the output error as a function of ANN weights. In the first phase, the weights of each neuron within the ANN are given initial values (Initialization). The network then feeds data from the input layer to the hidden layers and from the hidden layers to the output layer. In this approach, each neuron generates an output by multiplying the linear combination of its acquired inputs from the previous layer by the related weights. The activation function then affects the neuron's output, which maps it into the range [-1, 1] or [0, +1]. The final result is then sent to the next layer, and so on until the network reaches the output layer, where the ANN's estimated output value is compared to the actual output value. The computed error should be sent backward from the output layer to the input layer [15, 27].

$$x_j^l = \sigma\left(\sum_{i=1}^{N} w_{ji}^l x_i^{l-1}\right) \tag{12}$$

where $x^l{}_j$ is the final output of the neuron j in the lth layer, $x_i{}^{l-1}$ is the obtained input neuron j from the neuron i in the layer $l-1$, w_{ji} is the interconnected weight of the two neurons, σ is the activation function, and N is the number of neurons in the layer $l-1$ [15].

2.3. Numerical modeling

This study selects five airfoils from different airfoil families to simulate a wind turbine blade. These airfoils have been employed or can be used to design wind turbine blades. These airfoils have different geometries (symmetry, thin, and thick), which could provide a comprehensive study and compare the geometric effect on the efficiency of airfoils in a wind turbine. They are S809, DU84-32, NACA 63-415, FFA-W3-211, and Wortmann FX 66-S-196 with a chord of 1 m. Fig. 1 shows the geometry of the airfoils. This research used ANSYS commercial software and a developed ANN to explore the effect of geometry and aerodynamic parameters on the performance of each case.

A numerical study is computationally efficient when it is not dependent on the mesh resolution and has the lowest number of elements. In addition, the mesh structure should be able to capture any severe gradients in the solving equations. Fig. 2 shows the domain; there is a semicircle in front with a radius of 10 m and a rectangular with a length of 22 m in the back. The airfoil is located in the center of the semicircle. Since the boundary layer significantly affects the aerodynamic forces, the inflation mesh is applied on the airfoil surface and downstream. Fig. 2 presents how a dense mesh structure is used around the airfoil. In addition, Fig. 3 depicts that the solution is independent of the mesh structure. The grid with 124,033 elements is selected, associated with sufficient computational time and high accuracy.

In this study, the flow is considered an incompressible and isothermal fluid. The reference temperature and pressure are 25°C and 1 atm, respectively. The fluid characteristics are as follows: $\rho = 1.185$ kg/m^3, and $\mu = 1.831 \times 10^{-5}$ kg/m.s. The wind speed average at 40 m height is 5.76 m/s, which is collected from 18 wind farms. To provide a comprehensive study, this simulation is performed at different wind speeds (5, 7, 9, 11, and 13 m/s) with the angles of attack between -5° to 15°. Table 1 presents Reynolds numbers in this study.

The transition regime has a significant impact on the aerodynamic coefficients. Therefore, considering this regime should help to obtain accurate results. The transition shear stress transport (SST) turbulence model is used in this research. This turbulence model uses the turbulence frequency in the k-ω model on walls and the k-ϵ model in the bulk flow. A transfer function ensures a smooth transition between these two models. The SST model has been verified in several studies, and it shows the best accuracy for aerodynamic devices in the NASA technical memorandum [28]. The Michel method [25] predicts the transition Reynolds number. A user-defined formulation (UDF) is utilized to find the generated forces and consider three regimes (laminar, transition, and turbulent), which could improve the accuracy of the results.

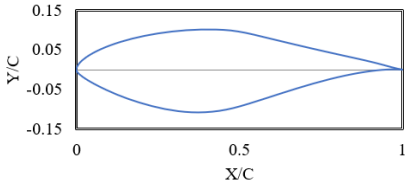

(a) NREL S809

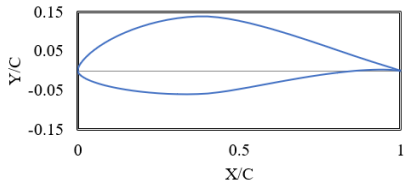

(b) Wortmann FX 66-S-196

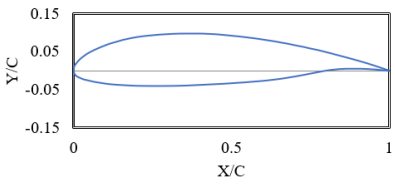

(c) DU 84-32

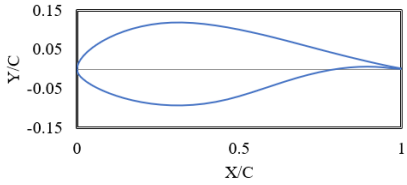

(d) FFA-W3-211

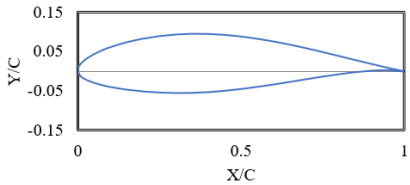

(e) NACA 63-415

Fig. 1 Selected airfoil geometry

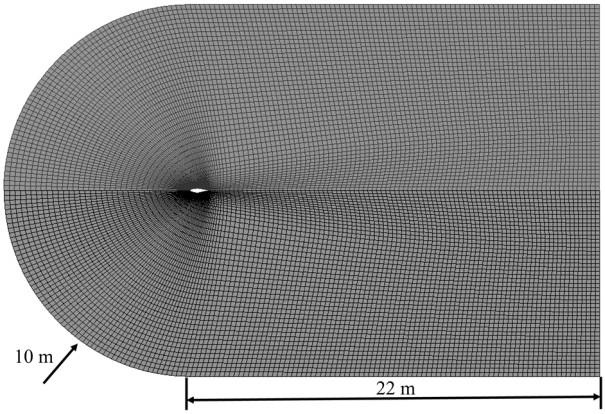

Fig. 2 Discretized domain and mesh structure

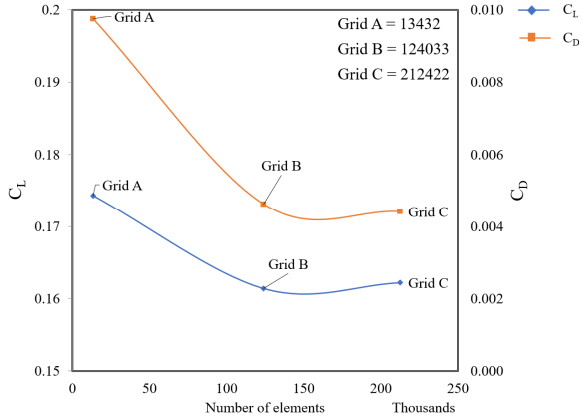

Fig. 3 Variation of lift and drag coefficients via the number of elements

Table 1 Reynolds number according to the selected wind speed

Wind speed (m/s)	Re × 10^5
5	3.23
7	4.53
9	5.79
11	6.95
13	8.21

The airfoil's wall is no-slip, and the side walls are symmetry planes from both sides. The upwind scheme method is used to reduce the errors and control the solutions. To ensure that the solution is converged, the RMS velocity fluctuation is assumed to be 10^{-5}. In addition, the turbulence intensity (the ratio of the RMS of the velocity fluctuations to the mean flow velocity) is considered medium, %5.

2.4. The developed ANN

The developed ANN in this study can be utilized as a robust predictive tool to assess the aerodynamic performance of wind turbines for experimental datasets. This study uses a dataset containing 525 CFD results to train the ANN. The dataset is divided into training (70%) and test (30%) datasets at random. The aerodynamic performance (sliding ratio) is the output in this network. With less than 2% error on the training set and less than 3% error on the test set based on Eq. (11), the developed ANN predicts the aerodynamic performance of selected airfoils [15].

To account for the problem's nonlinearity, two hidden layers are chosen. There is no reason to unnecessarily increase the number of hidden layers or neurons because two hidden layers are enough for any ANNs to fit any nonlinear function. An excessive number of neurons can lead to overfitting concerns [26]. The neural network is trained 500 times, from one neuron to 500 neurons per layer, to find the optimum number of neurons in each hidden layer. In addition, the RMS of error is determined simultaneously for the training and test datasets. Fig. 4 shows that seven neurons in each hidden layer should be the best network. This number of neurons yields the smallest difference between training and test RMS errors and a local minimum of the training RMS error. This produces well-fitted results on the training dataset, prevents overfitting, and allows the network to generalize [15].

Figs. 5-6 compare the predicted sliding ratio using ANN to the obtained CFD sliding ratio for training and test data points. According to the results, the trained ANN has an average prediction accuracy of 98.36%. Furthermore, the test results demonstrate that the average prediction accuracy is 97.79 %. The findings support the model's capacity to generalize to other datasets. It can be conducted parametric analyses using the developed ANN as a predictive model based on the ANN accuracy assessment [15].

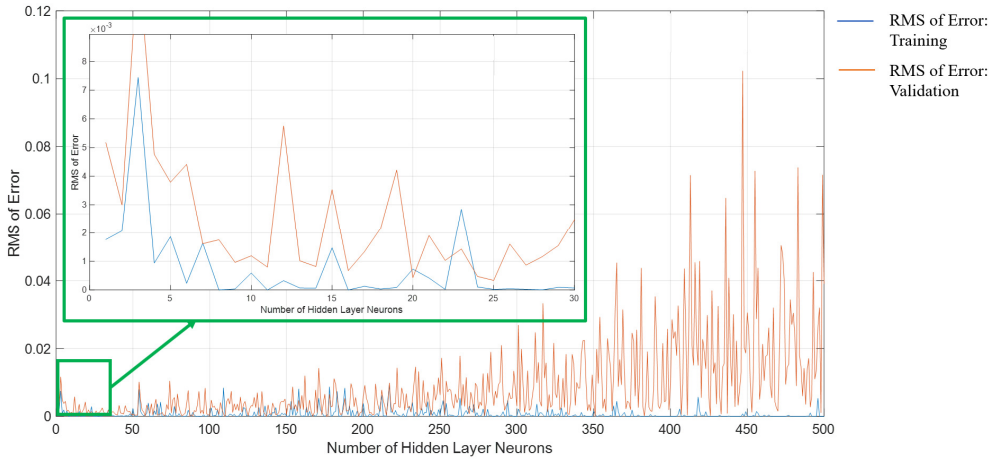

Fig. 4 Number of hidden layer neurons vs. RMS

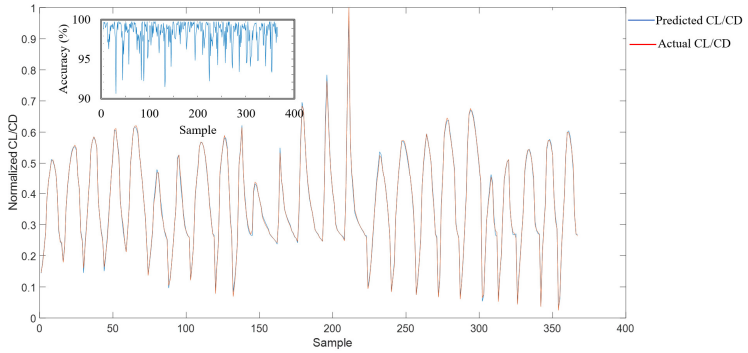

Fig. 5 Train vs. actual aerodynamic performance results

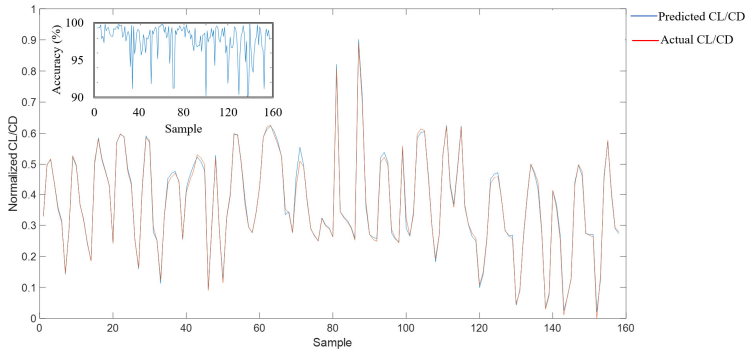

Fig. 6 Test vs. actual aerodynamic performance results

2.5. *Validation*

To verify this study, the simulated results of the NREL S809 airfoil are compared to the experimental data from laboratory tests at the Delft University of Technology [29]. The airfoil chord is 600 mm, and the Reynolds number is 2×10^6. The numerical lift and drag coefficients are compared to the experimental results in Fig. 7. In addition, Fig. 8 shows the pressure distribution results on the airfoil. These comparisons indicate the agreement between this study and the experimental results.

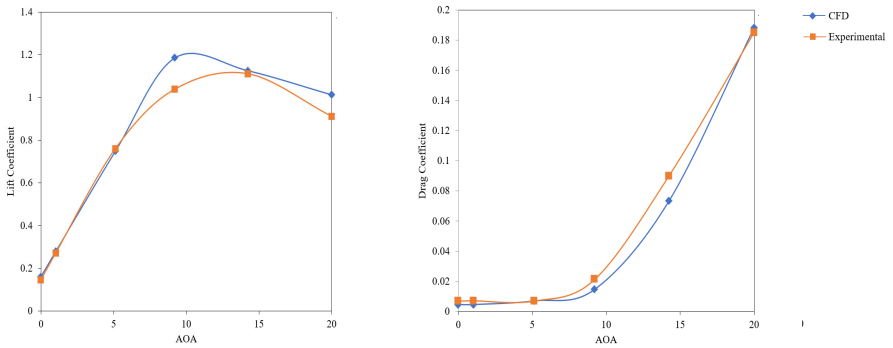

(a) Lift coefficient validation (b) Drag coefficient validation

Fig. 7 Experimental [29] and numerical comparison at different AOA

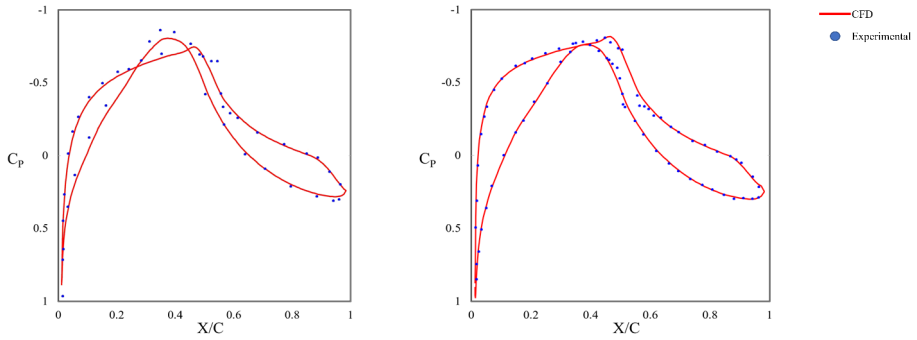

(a) AOA = 0° (b) AOA = 1.02°

Fig. 8 Experimental [29] and numerical pressure distribution at different AOA

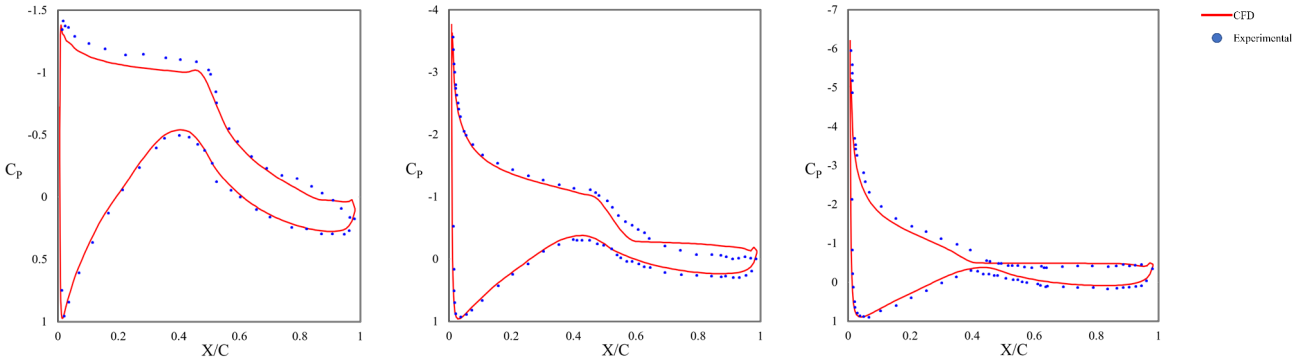

(c) AOA = 5.13° (d) AOA = 9.22° (e) AOA = 14.24°

Fig. 8 Experimental [29] and numerical pressure distribution at different AOA (continued)

3. Results and Discussion

Figs. 9-13 show the sliding ratio behavior versus AOA at different wind speeds. They illustrate that the sliding ratio enhances with increasing the wind speed in all cases. The maximum sliding ratio occurs at different AOA for each airfoil. They present that changing the sliding ratio follows the same trend for all cases: it ascends until it reaches a maximum value, then descends slightly to the same value. This convergence occurs at a higher AOA, and the value is different in each case study. These figures show that most sliding ratio changes happen between 0° to 10° of AOA, except for the airfoil FX66-S-196. This airfoil encounters the most variation of the sliding ratio between -5° to 0° of AOA.

The geometry parameters affecting the aerodynamic coefficients are leading-edge, mean camber line, trailing edge, and maximum thickness. The lift coefficient increases in the negative small AOA range, and the drag coefficient decreases. Therefore, DU84-132 and FX66-S-196 airfoils have the highest sliding ratio because of their curved shape. In contrast, if an airfoil has a symmetrical profile like NREL S809, the pressure difference between the upper and lower edges is low. Hence, the sliding ratio has a small value at 0° AOA. In addition, the sliding ratio increases by increasing the wind speed at the same AOA. Both lift and drag coefficients increase with the increase of AOA, but the lift coefficient increase rate is higher than the drag coefficient at a constant wind speed. This situation continues until the lift coefficient rate declines, but the drag coefficient still rises, resulting in decreasing the sliding ratio.

The maximum sliding ratio should be found to achieve the maximum power from a wind turbine. Indeed, the lift coefficient is a vital factor in rotating the rotor, and the drag coefficient is a factor of friction and has a negative impact on the efficiency of blades. Then, the maximum lift and minimum drag coefficients are an objective for harvesting the maximum energy from a wind turbine. FX-66-S-196, DU 84-132, and NACA 63-415 airfoils have median sliding ratios; on the other hand, FFA-W3-211 and NREL S809 airfoils have the lowest sliding ratio because of their symmetric airfoil shape.

Table 2 shows the optimum AOA range to achieve the maximum energy at different wind speeds. This range for airfoil FX66-S-196 is from -4° to -2°. The optimum range is between 3° and 7° for the other airfoils. The best AOA is discovered in the negative zone of the airfoil FX66-S-196, since the airfoil's maximum thickness is located at the top of the chord. While the airfoil's maximum thickness is located in the middle of the airfoil, the optimum AOA range happens in a positive zone. Therefore, it could guide selecting the best airfoil according to the sliding ratio and the range of AOA at each speed.

The results show that the performance of an airfoil depends on the AOA and geometry. Furthermore, they indicate that AOA has a dominant influence on choosing the best airfoil, while wind speed does not have a similar impact. The perfect airfoils in the AOA of 0°, 1°, and 2° are FX66-S-196, DU84-132, and NACA63-415. Thus, if the airfoil's maximum thickness is located between 40% and 50% of the chord, the best range of AOA happens in the small positive range. On the other hand, while the airfoil has a maximum thickness from 20% to 40% of the chord, the optimal AOA has a small negative value.

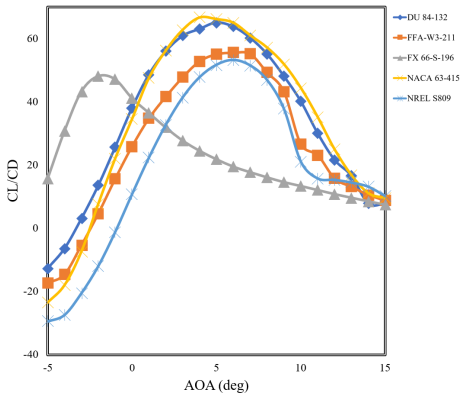

Fig. 9 Sliding ratio vs. AOA at the wind speed of 5 m/s

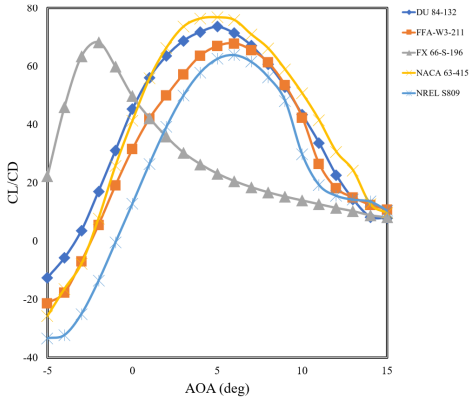

Fig. 10 Sliding ratio vs. AOA at the wind speed of 7 m/s

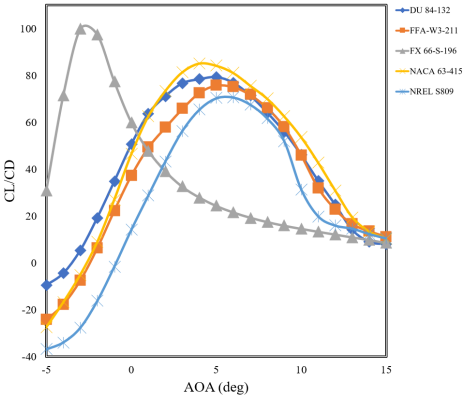

Fig. 11 Sliding ratio vs. AOA at the wind speed of 9 m/s

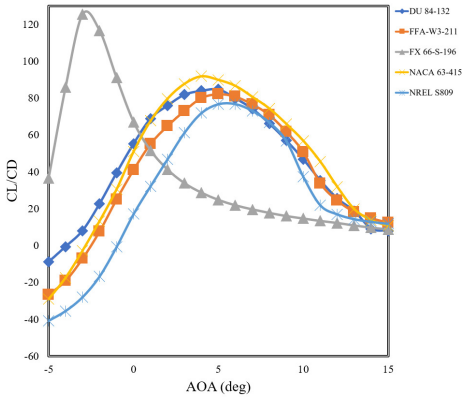

Fig. 12 Sliding ratio vs. AOA at the wind speed of 11 m/s

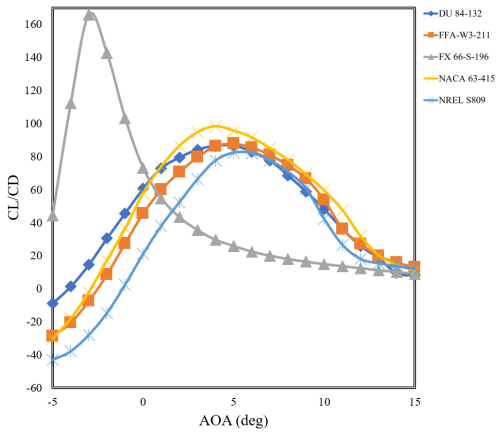

Fig. 13 Sliding ratio vs. AOA at the wind speed of 13 m/s

Table 2 Optimum range of AOA for different airfoils

Wind speed	DU84-32	FFA-W3-211	FX 66-S-196	NACA 63-415	S809
5	5	6	-2	4	6
7	5	6	-2	4	6
9	5	5	-3	4	6
11	5	5	-3	4	6
13	5	5	-3	4	6

A larger stall angle creates a desirable condition in an aerodynamics study. Whatever this angle has a more considerable value, the stall phenomenon occurs later. The velocity and pressure distributions on the selected airfoils at the wind speed of 7 m/s and AOA of 0° are shown in Figs. 14-18. The pressure on the bottom surface is more than the upper surface in all airfoils, so the positive lift force causes the blades to rotate. The pressure increases from a minimum to a maximum value on the trailing edge. The adverse pressure gradient occurs in this region. If the adverse pressure gradient rate increases, transition and separation occur in the boundary layer.

The pressure at the trailing edge depends on the thickness and shape of the airfoil. The stagnation occurs close to the trailing edge when the velocity is zero, and C_p equals 1. According to Figs. 14-18, where the flow accelerates on the airfoil, the pressure reduces to low values; thus, C_p reaches zero and negative values. Then, the flow declines, the pressure increases, and the absolute value of C_p decreases.

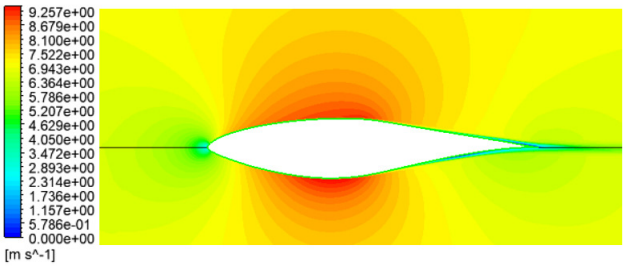

(a) Velocity contours

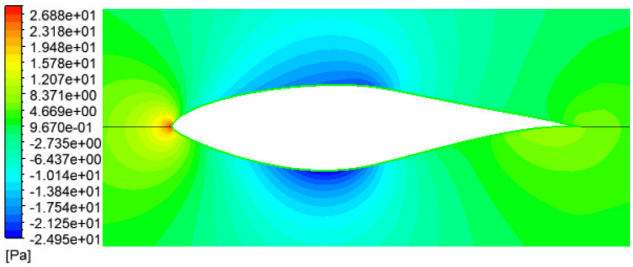

(b) Pressure contours

Fig. 14 Flow contours on the NREL S809 airfoil at the wind speed of 7 m/s and AOA of 0°

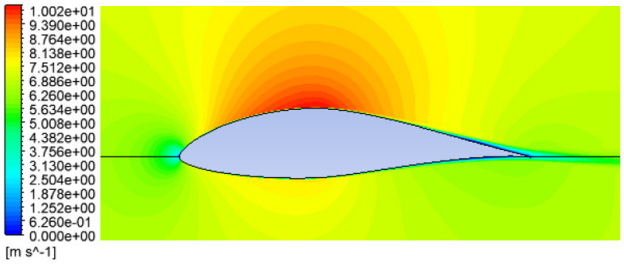

(a) Velocity contours

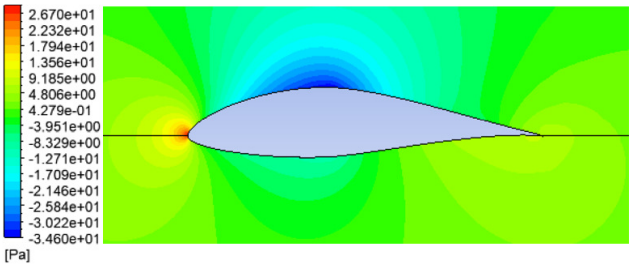

(b) Pressure contours

Fig. 15 Flow contours on the FX66-S-196 airfoil at the wind speed of 7 m/s and AOA of 0°

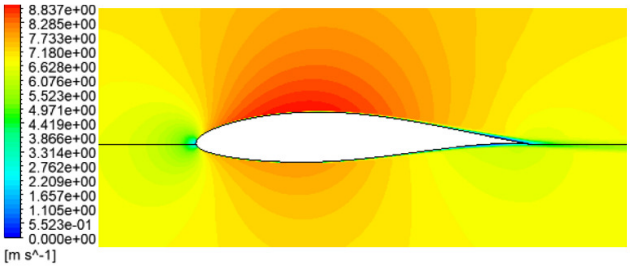

(a) Velocity contours

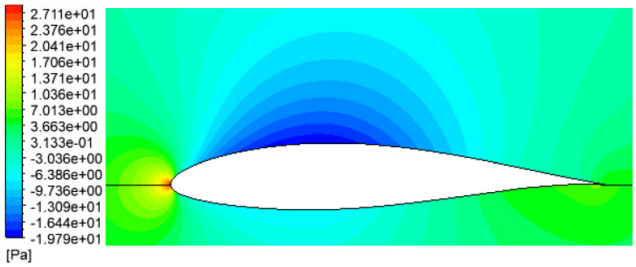

(b) Pressure contours

Fig. 16 Flow contours on the NACA63-415 airfoil at the wind speed of 7 m/s and AOA of 0°

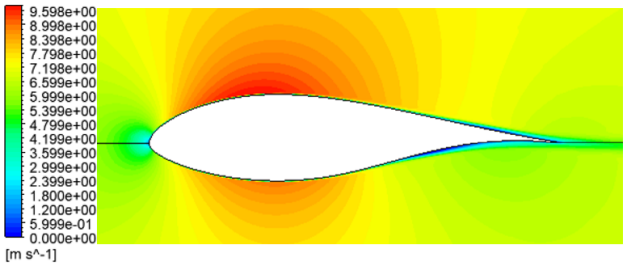

(a) Velocity contours

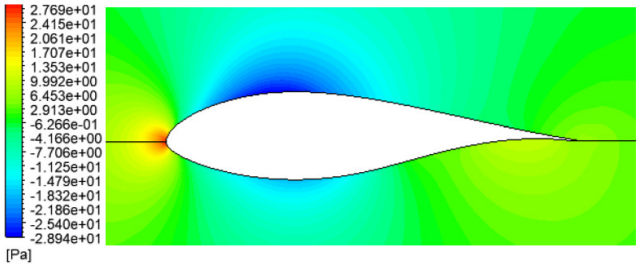

(b) Pressure contours

Fig. 17 Flow contours on the FFA-W3-212 airfoil at the wind speed of 7 m/s and AOA of 0°

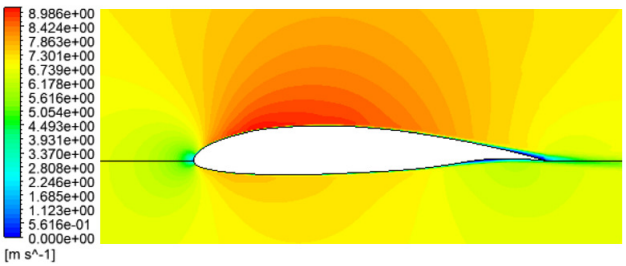

(a) Velocity contours

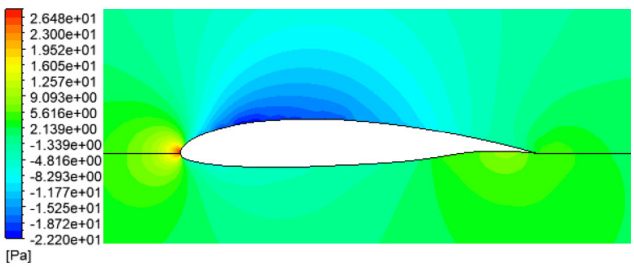

(b) Pressure contours

Fig. 18 Flow contours on the DU84-132 airfoil at the wind speed of 7 m/s and AOA of 0°

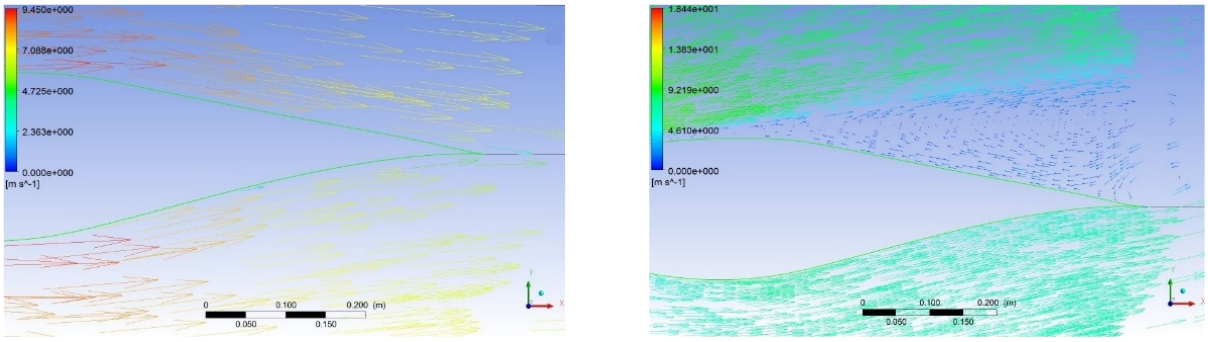

(a) AOA = 0° (b) AOA = 15°

Fig. 19 Velocity vector on the NREL S809 airfoil at the wind speed of 7 m/s

The pressure coefficient is led towards negative values by increasing the wind speed. Furthermore, the flow reduces on the upper surface at the trailing edge due to mixing the flow on the bottom surface. When the adverse pressure has been boosted, the separation point moves toward the front of the airfoil, so the separation happens faster in a larger AOA. According to the pressure distribution, the pressure coefficient is positive on the upper surface and negative on the bottom when the AOA is smaller than zero. The pressure on the top surface is similar to the pressure on the bottom surface when AOA is zero for symmetrical airfoils. In addition, the pressure coefficient is negative on the upper surface and positive on the bottom surface when AOA is above zero. Therefore, the lift coefficient moves upward. On the other hand, the pressure difference between the upper and lower surfaces increases at a higher AOA.

Fig. 19 indicates the separation on the NREL S 809 for two AOA. Flow separation occurs by enlarging AOA, which has a remarkable impact on aerodynamic coefficients. According to the results, the sliding ratio decreases, and flow separation happens by increasing AOA. The extreme pressure difference between the upper and lower surfaces causes flow separation. This pressure difference causes destructive aerodynamic phenomena such as vortex. Besides, the resultant reaction forces cause an intense vibration of the airfoil, which could be known as flutter.

The flow begins to leave the upper surface from the transition point to the separation point. The flow completely separates by reaching the separation point. This point moves to the front edge of the airfoil by increasing the AOA. The thinned boundary layer can prevent separation by reducing the pressure drop in the reverse region. Furthermore, a curved forehead airfoil can minimize the possibility of flow separation.

4. Conclusions

This work studied the aerodynamic performance of several airfoils used in wind farms. AOA and wind speed range from -5° to 15° and 5 to 13 m/s are assumed, respectively. Furthermore, the turbulence model by considering the transition from laminar to turbulent flow is utilized in the boundary layer. A developed ANN is used to offer a thorough parametric evaluation of the performance of wind turbines based on selecting airfoil.

The results illustrate that the AOA has a noticeable impact on the airfoil performance, and there is an analogy between the geometry and efficiency. The optimum AOA has a small positive value when the airfoil's maximum thickness is located in 40% to 50% of the chord. On the other hand, while the airfoil has a maximum thickness in 20% to 40% of the chord, the optimal AOA has a small negative value. Furthermore, when the AOA is smaller than zero, the pressure coefficient on the upper surface is positive and negative on the bottom surface, so the lift force is toward down. When the AOA is zero, the pressure coefficients are almost the same on upper and lower surfaces for a symmetrical airfoil. In addition, the flow separation occurs by increasing the AOA in all airfoils, which impacts aerodynamic coefficients. Moreover, it is concluded that the airfoil FX66-S-196 and NACA 63-415 could gain the maximum power from wind in a negative and positive AOA, respectively. They are the best among these airfoils in working at a wide range of wind speeds.

Nomenclature

C_L	Lift coefficient
C_D	Drag coefficient
L	Lift force
D	Drag force
ρ	Density
V	Wind speed
A	Cross-section area
ε	Sliding ratio
u	Velocity component
v	Velocity component
p	Pressure
μ	dynamic viscosity
Re_x	Reynolds number from the stagnation point
Re_{trans}	Momentum thickness Reynolds number
n	Number of samples in the training dataset
e_k	Error at the output layer
RMS_{error}	Root mean square of the error at the output layer

Conflicts of Interest

The authors declare no conflicts of interest.

References

[1] A. Shourangiz-Haghighi, et al., "State of the Art in the Optimisation of Wind Turbine Performance Using CFD," Archives of Computational Methods in Engineering, vol. 27, no. 2, pp. 413-431, 2020.

[2] M. R. Aligoodarz, et al., "Improved Criteria for Stall-Free Preliminary Design of Axial Compressor of Aero Gas Turbine Engines," Proceedings of the Institution of Mechanical Engineers, Part G: Journal of Aerospace Engineering, vol. 233, no. 9, pp. 3286-3297, July 2019.

[3] B. Hand, et al., "Aerodynamic Design and Performance Parameters of a Lift-Type Vertical Axis Wind Turbine: Comprehensive Review," Renewable and Sustainable Energy Reviews, vol. 139, Article no. 110699, April 2021.

[4] J. F. Manwell, et al., Wind Energy Explained: Theory, Design and Application, 2nd ed., Massachusetts: John Wiley & Sons Ltd, 2009.

[5] M. A. Sayed, et al., "Aerodynamic Analysis of Different Wind-Turbine-Blade Profiles Using Finite-Volume Method," Energy Conversion and Management, vol. 64, pp. 541-550, December 2012.

[6] X. Hua, et al., "Wind Turbine Bionic Blade Design and Performance Analysis," Journal of Visual Communication and Image Representation, vol. 60, pp. 258-265, April 2019.

[7] Y. B. Chen, et al., "Two-Way Fluid-Structure Interaction Simulation of a Micro Horizontal Axis Wind Turbine," International Journal of Engineering and Technology Innovation, vol. 5, no. 1, pp. 33-44, January 2015.

[8] D. D. Dai, et al., "The Numerical Simulation of Aerodynamic Performance for Wind Turbines' Blade Wheel," Applied Mechanics and Materials, vol. 34, pp. 1761-1764, 2010.

[9] S. Le Clainche, et al., "A Reduced Order Model to Predict Transient Flows around Straight Bladed Vertical Axis Wind Turbines," Energies, vol. 11, no. 3, Article no. 566, March 2018.

[10] S. D. Pesmajoglou, et al., "Prediction of Aerodynamic Forces on Horizontal Axis Wind Turbines in Free Yaw and Turbulence," Journal of Wind Engineering and Industrial Aerodynamics, vol. 86, no. 1, pp. 1-14, May 2000.

[11] M. J. Churchfield, et al., "A Numerical Study of the Effects of Atmospheric and Wake Turbulence on Wind Turbine Dynamics," Journal of Turbulence, vol. 13, no. 14, pp. 1-32, 2012.

[12] M. Ahmadi-Baloutaki, et al., "The Role of Free-Stream Turbulence on Flow Evolution in the Wake of a VAWT Blade," Wind Engineering, vol. 37, no. 4, pp. 401-420, August 2013.

[13] S. Wang, et al., "Turbulence Modeling of Deep Dynamic Stall at Relatively Low Reynolds Number," Journal of Fluids and Structures, vol. 33, pp. 191-209, August 2012.

[14] J. Yao, et al., "Numerical Simulation of Aerodynamic Performance for Two Dimensional Wind Turbine Airfoils," Procedia Engineering, vol. 31, pp. 80-86, 2012.
[15] M. Moshtaghzadeh, et al., "Artificial Neural Network for the Prediction of Fatigue Life of a Flexible Foldable Origami Antenna with Kresling Pattern," Thin-Walled Structures, vol. 174, Article no. 109160, May 2022.
[16] J. X. F. Ribeiro, et al., "Prediction of Pressure Gradient in Two and Three-Phase Flows in Horizontal Pipes Using an Artificial Neural Network Model," International Journal of Engineering and Technology Innovation, vol. 9, no. 3, pp. 155-170, May 2019.
[17] J. Nielson, et al., "Using Atmospheric Inputs for Artificial Neural Networks to Improve Wind Turbine Power Prediction," Energy, vol. 190, Article no. 116273, January 2020.
[18] J. Luna, et al., "Wind Turbine Fatigue Reduction Based on Economic-Tracking NMPC with Direct ANN Fatigue Estimation," Renewable Energy, vol. 147, pp. 1632-1641, March 2020.
[19] A. Saenz-Aguirre, et al., "Optimal Wind Turbine Operation by Artificial Neural Network-Based Active Gurney Flap Flow Control," Sustainability, vol. 11, no. 10, Article no. 2809, May 2019.
[20] M. E. M. Salem, et al., "Application of Neural Network Fitting for Pitch Angle Control of Small Wind Turbines," IFAC-PapersOnLine, vol. 54, no. 14, pp. 185-190, 2021.
[21] L. Cappugi, et al., "Machine Learning-Enabled Prediction of Wind Turbine Energy Yield Losses Due to General Blade Leading Edge Erosion," Energy Conversion and Management, vol. 245, Article no. 114567, October 2021.
[22] H. K. Versteeg, et al., An Introduction to Computational Fluid Dynamics: The Finite Volume Method, 2nd ed., Glasgow: Pearson Education Limited, 2007.
[23] J. Johansen, Prediction of Laminar/Turbulent Transition in Airfoil Flows, Roskilde: Risø National Laboratory, 1997.
[24] G. J. Hokenson, "Consistent Integral Thickness Utilization for Boundary Layers with Transverse Curvature," AIAA Journal, vol. 15, no. 4, pp. 597-600, April 1977.
[25] T. Burton, et al., Wind Energy Handbook, 2nd ed., New Delhi: Wiley, 2011.
[26] W. He, et al., "State of Charge Estimation for Li-Ion Batteries Using Neural Network Modeling and Unscented Kalman Filter-Based Error Cancellation," International Journal of Electrical Power and Energy Systems, vol. 62, pp. 783-791, November 2014.
[27] I. A. Basheer, et al., "Artificial Neural Networks: Fundamentals, Computing, Design, and Application," Journal of Microbiological Methods, vol. 43, no. 1, pp. 3-31, December 2000.
[28] J. E. Bardina, et al., "Turbulence Modeling Validation, Testing, and Development," Ames Research Center, Technical Report A-976276, April 1997.
[29] D. M. Somers, "Design and Experimental Results for the S809 Airfoil," National Renewable Energy Laboratory, Technical Report NREL/SR-440-6918, January 1997.